

# Premature breakaway oxidation of ferritic stainless steels triggered by austenitization



Citation for the original published paper (version of record):

Chyrkin, A., Froitzheim, J. (2025). Premature breakaway oxidation of ferritic stainless steels triggered by austenitization. Corrosion Science, 256. http://dx.doi.org/10.1016/j.corsci.2025.113260

N.B. When citing this work, cite the original published paper.

research.chalmers.se offers the possibility of retrieving research publications produced at Chalmers University of Technology. It covers all kind of research output: articles, dissertations, conference papers, reports etc. since 2004. research.chalmers.se is administrated and maintained by Chalmers Library

ELSEVIER

Contents lists available at ScienceDirect

# Corrosion Science

journal homepage: www.elsevier.com/locate/corsci





# Premature breakaway oxidation of ferritic stainless steels triggered by austenitization

Anton Chyrkin \* D, Jan Froitzheim

Chalmers University of Technology, Department of Chemistry and Chemical Engineering, Kemivägen 10, Gothenburg 412 96, Sweden

#### ABSTRACT

Thin foils (0.2–0.3 mm thick) of commercially available ferritic stainless steels Crofer 22 APU and Crofer 22 H have been oxidized in air for up to 2000 h at 900, 950, 1000, and 1050 °C. Both steel grades suffered from premature breakaway oxidation, despite the remnant Cr content in the foils being 18–20 wt% at the oxide-metal interface. Crofer 22 APU was found to be more susceptible to breakaway oxidation compared to Crofer 22 H. The classical lifetime prediction tools systematically overestimated the time to breakaway. Premature breakaway oxidation above 900 °C is demonstrated to be triggered by austenitization (the  $\alpha$ -to- $\gamma$  transformation in the Fe-Cr system) occurring in the Cr-depleted corners and edges of the foils. A novel lifetime model accounting for austenitization and geometrical constraints was introduced and validated.

#### 1. Introduction

Ferritic stainless steels based on FeCr [1] and FeCrAl [2,3] alloy systems form a special family of high-alloyed metallic materials. FeCrAl-based alloys are known for their superior oxidation resistance up to 1200 °C and find their application mainly as structural materials for heating elements, catalyst support [3], recently also additively manufactured (AM) components [4,5]. Excellent oxidation properties of FeCrAls rely on the formation of a well-adherent and slowly growing, protective  $\alpha\text{-Al}_2O_3$  scale [6,7]. The FeCr-based ferritic steels containing 12-30 wt% Cr form  $\text{Cr}_2O_3$  scales, which limits their maximum operating temperature to 900 °C due to relatively high oxide growth rates [1] and eventually intense oxide spallation during thermal cycling [8]. The chromia-forming ferritic steels haven been used in e.g. automotive exhaust systems but gained much attention as interconnect material for solid oxide fuel cells (SOFCs) and electrolyzer (SOEC) operating at 600-850 °C [1].

Both FeCrAl- and FeCr-based steels are often used for manufacturing thin-walled components such as tenths of a mm thick sheets, foils, wires, porous metal foams, etc. These parts have a limited chemical lifetime in service due to a critical oxidation-induced Al- or Cr-depletion followed by breakaway oxidation, i.e., extremely rapid growth of Fe-rich oxides [9]. Breakaway oxidation is known to start at edges and corners of specimen/part due to a higher surface-to-volume ratio and, hence, a locally higher depletion rate [10,11].

In the 1990s, a simple mathematical mass-balance model (MB) was developed by Quadakkers for FeCrAls to quantitatively predict a time to

breakaway as a function of temperature (parabolic rate constant,  $k_p$  or  $k_c$  if expressed in terms of metal recession, or just k for subparabolic kinetics), specimen thickness and Al-content [12]. The model was based on equating the experimentally measurable oxide growth rate to the total amount of consumed Al in the specimen assuming that the Al-concentration across the specimens remains uniform due to a relatively low  $k_c/D$  ratio. Here  $k_c$  is the parabolic rate constant in terms of metal recession and D the diffusion coefficient of the scale forming element. For FeCrAl materials this approach has been successfully demonstrated to accurately predict a chemical life of FeCrAl-based alloy with  $k_c/D \sim 10^{-5}$ , i.e., fast Al diffusion in comparison to scale growth.

An alternative way to mathematically describe the depletion process in a thin-walled component is the diffusion analysis proposed by Whittle [13], corrected by Cowen and Webster [14] and further applied to mainly austenitic steels [15,16] and Ni-base alloys [17]. This model is a generalized solution of a diffusion problem and does not require the presumption of a uniform concentration profile. In [18], the Whittle depletion (WD) model was demonstrated to converge to the mass-balance (MB) equation when the  $k_{\rm c}/D$  ratio is negligible, i.e., faster diffusion and a flat concentration profile. In other words, the mass-balance model (MB) is a limited case of the generalized Whittle's solution and will be termed as Reduced Whittle (RW) model in this work. A detailed derivation of the models can be found in the Data Supplement.

The mass-balance model was further applied to FeCr-based chromiaforming ferritic such as Crofer 22 APU at 900 °C [19]. The  $k_c/D$  ratio for FeCr is higher ( $\sim 10^{-4}$ ) which is reflected in a slight Cr gradient towards

E-mail address: chyrkin@chalmers.se (A. Chyrkin).

<sup>\*</sup> Corresponding author.

the oxide-alloy interface (no more than 2 wt% difference between the surface and the bulk) [19]. Furthermore, parabolic rate constants for FeCr-based ferritic alloys have been shown to increase with a decreasing specimen thickness due to a plastic deformation of the specimens [20, 21]. Nevertheless, the mass-balance model accurately enough predicted time to breakaway for FeCr-based alloys. The mathematical expression was the same while the only difference between the FeCrAl and FeCr cases was the critical concentration of the scale-forming element. Thin foils of FeCrAl are generally considered to run into breakaway oxidation once Al is completely exhausted, i.e., depleted to zero,  $C_{Al}^{crit}=0$  wt%. At the same time, FeCr alloys are reported to fail at a relatively high residual Cr content,  $C_{Cr}^{crit}=8$ –16 wt% [19,22,23]. Hence, a critical Cr concentration of  $\sim$ 10 % is commonly accepted although this limit lacks a mechanistic foundation.

Recently, Chyrkin et al. [24,25] demonstrated that breakaway oxidation of FeCr-base alloys is triggered by Cr-depletion driven austenitization at 900°C. The working hypothesis for the present study is that the  $\alpha$ -to- $\gamma$  phase-transformation occurring e.g. between 10.7 and 12.2 wt % at 900 °C and 13–14 wt% at 1000 °C according to the Fe-Cr phase diagram [26] is responsible for the premature oxidation-induced failure of chromia forming ferritic stainless steels. Apart from the metallurgical considerations, multiple studies provide evidence of a better oxidation performance of ferritic stainless steels alloyed with the  $\alpha$ –BCC stabilizing elements such as W, Nb, Si, etc.

For instance, 0.2 mm thick foils of the precipitation and solution hardened Crofer 22 H demonstrate steady-state parabolic kinetics over 1000 h at 900 °C in air while those of Crofer 22 APU run into breakaway after 300 h [27]. Hence, a premature failure of Crofer 22 APU compared to Crofer 22 H might be related to the  $\alpha$ -to- $\gamma$  phase-transformation in Crofer 22 APU, which would explain its occurrence at  $C_{Cr}^{crit} \approx 10$  wt% at 900 °C as reported in [19,22,23].

The goal of the present work is to investigate the role of the  $\alpha\text{-to-}\gamma$  phase-transformation in FeCr-based alloys, specifically in steel grades Crofer 22 APU and Crofer 22 H, as well as the related chemical failure of these materials during high-temperature exposures at 900  $^{\circ}\text{C}$  and above, develop and validate a lifetime prediction tool considering the possibility of austenitization, and finally explore potential alloying strategies to extend the chemical life of ferritic stainless steels.

# 2. Experimental

#### 2.1. Materials

The 0.3 mm thick sheets of Crofer 22 APU and Crofer 22 H were supplied by VDM Metals. Their chemical compositions are listed in Table 1. Test coupons measuring  $15\times15~\text{mm}^2$  were cut from the sheets and ground with SiC papers to 0.3 and 0.2 mm thickness and P1200 surface finish. Several rectangular specimens were rounded by grinding to eliminate sharp corners and thereby explore the effect of specimen geometry on lifetime. The samples were degreased with acetone and ethanol prior to exposure.

# 2.2. Exposures

Exposure of the steel samples were carried out in horizontal tubular furnace with an inner diameter of 46 mm. The test coupons were hanged through a 2 mm orifice drilled in each coupon on a 1 mm thick alumina rod in a boat-shaped alumina crucible or placed onto an alumina plate

with 0.5 mm thick and 1.0 mm deep slots. The exposures were carried out in stagnant lab air. The specimen holder was immediately introduced into the hot zone of the furnace and readily moved into the cold zone of the furnace after the dwell time (mainly 48 h). All oxidation experiments were performed with 3 test coupons. Mass gains were measured at every cooling step with Mettler Toledo microbalance. The weight measurements were very reproducible in the protective mode, i. e., parabolic growth of  $\rm Cr_2O_3$ . The standard deviation did not exceed 0.02 mg/cm². After the onset of breakaway, the standard deviation increased to 0.3 mg/cm².

The 0.2 mm thick specimen were tested for up to 2000 h at 900°C. Testing of the Crofer 22 APU samples was interrupted after 1000 h due to severe breakaway corrosion at the edges of the test coupons. The 0.3 mm thick foils were tested at 950, 1000 and 1050 °C for up to 1200 h

#### 2.3. Post-exposure characterization

After the exposures, cross-sections were prepared using a Leica TIC 3X broad ion beam (BIB) for SEM-EDX analysis. An FEI ESEM QUANTA 200 equipped with an Oxford X-max 80 EDX detector was used for cross-sectional SEM-EDX analyses of the BIB cross-sections. The error margin of EDX analysis for Cr is estimated at 0.1 wt%. Selected specimens were cold mounted in epoxy resin to metallographically prepare full-length cross-sections and investigate the corroded edges of the foils. The cold-mounted specimens were gold-coated and electroplated with Ni prior to mounting. The mounted specimens were mechanically ground to 4000 grit, polished with diamond pastes to 0.25  $\mu m$  surface finish and finally polished with a solution of colloidal silica. Selected cross-sectioned specimens were chemically etched with a KALLING 1 solution (CuCl2, HCl and ethanol, Morphisto GmbH, Offenbach am Main, Germany) and analyzed with the optical microscope Zeiss Axio Observer.

#### 3. Results

# 3.1. Oxidation at 900 °C

Fig. 1 shows oxygen uptake for 0.2 mm thick foils of Crofer 22 APU and Crofer 22 H during air exposure at 900  $^{\circ}$ C. For up to 700 h, both steel grades demonstrate a protective behavior and parabolic oxidation kinetics. The measured oxidation rate for Crofer 22 APU is in very good agreement with the previously reported data [19]. Crofer 22 APU oxidizes slightly faster than Crofer 22 H, in agreement with the data acquired at 800  $^{\circ}$ C [20]. After 700 h, oxidation of Crofer 22 APU dramatically accelerates while Crofer 22 H continues to oxidize parabolically up to 2000 h. The accelerated oxidation of Crofer 22 APU is related to occurrence of breakaway, i.e., rapid growth of Fe-rich oxides at the edges of the foil specimen.

Fig. 2 demonstrates BSE SEM images of cross-sectioned oxide scales grown on Crofer 22 APU and Crofer 22 H after 1000 h air oxidation at 900 °C. Both steel grades form a duplex oxide scale consisting of an outer thin (1–2  $\mu m$ ) layer of Mn-rich spinel (Mn,Cr)<sub>3</sub>O<sub>4</sub> and a layer of Cr<sub>2</sub>O<sub>3</sub>, 16.1  $\pm$  0.8  $\mu m$  thick for Crofer APU and 12.4  $\pm$  0.4  $\mu m$  thick for Crofer 22 H. Crofer 22 APU grew a thicker Cr<sub>2</sub>O<sub>3</sub> with characteristic oxide intrusions into the steel substrate while Crofer 22 H tends to form a smoother and thinner Cr<sub>2</sub>O<sub>3</sub> scale. Crofer 22 H reveals characteristic intermetallic precipitates segregated at the oxide-metal interface. These precipitates are Laves-phases which are common for the Crofer 22 H

Table 1 Chemical composition in wt% of Crofer 22 APU and Crofer 22 H used in the present study.

	Fe	Cr	Mn	Si	Ti	W	Nb	С	La
Crofer 22 APU	Bal.	22,9	0,38	0,01	0,06	-	-	0004	0,09
Crofer 22 H	Bal.	22,6	0,43	0,24	0,06	1,97	0,49	0009	0,05

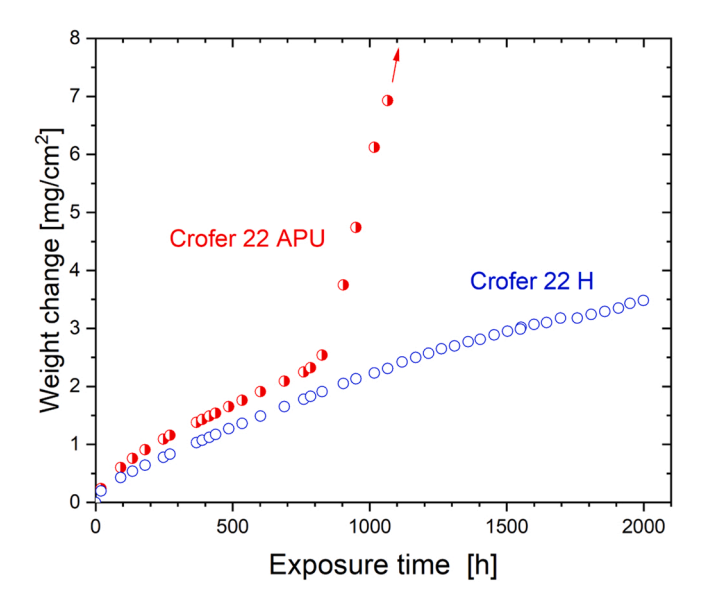


Fig. 1. Weight change for 0.2 mm thick foils of steel grades Crofer 22 APU and Crofer 22 H during discontinuous air oxidation for up to 2000 h at  $900^{\circ}$ C.

microstructure and tend to precipitate at alloy grain boundaries [20,28] and oxide-metal interface [29]. The specimen edges shown in Fig. 2c, d demonstrate a significant difference in oxidation behaviour between Crofer 22 APU and Crofer 22 H at 900 °C. While Crofer 22 APU suffered from massive breakaway oxidation of the specimen edge, Crofer 22 H demonstrated a fully protective oxidation behaviour and remained protective after 2000 h of exposure (similar oxide scale morphology to Fig. 2d, not shown here). At the same time, neither steel revealed any sign of breakaway oxidation in the middle of the specimen.

Temporal evolution of oxide scale thickness at 900  $^{\circ}$ C measured in BSE images is illustrated in Fig. 3. The scaling kinetics for Crofer APU are slightly faster compared to Crofer 22 H in agreement with the thermogravimetric data (Fig. 1). This effect is well documented for Crofer steel grades and is attributed to a higher creep rate of Crofer 22 APU compared to the solution hardened and precipitation strengthened Crofer 22 H. It was suggested [30] that compressive stresses in the  $\text{Cr}_2\text{O}_3$  scale affect the concentration of point defects in the oxide. In this context, it was reported that a  $\text{Cr}_2\text{O}_3$  scale formed under lower stress on thin Crofer 22 APU thickens faster [20].

#### 3.2. Oxidation at 950 °C

Fig. 4 shows weight change curves for 0.3 mm thick foils of Crofer 22 APU and Crofer 22 H during air exposure at 950  $^{\circ}$ C. This time, both steel grades suffer from breakaway oxidation: Crofer 22 APU after approx. 200–250 h while Crofer 22 H after 1200 h.

Fig. 5 demonstrates BSE SEM images of cross-sectioned Crofer 22 APU and Crofer 22 H foils after 1000 h of discontinuous air oxidation at 950 °C. The oxide scales grown at 950 °C are similar to those formed at 900 °C (Fig. 2): i) the  $\rm Cr_2O_3$  scale is overlaid by an outer layer of Mn-rich spinel, ii) the  $\rm Cr_2O_3$  scale formed on Crofer 22 APU has more pronounced oxide intrusion into the metal than the scale on Crofer 22 H. The voids (Fig. 5a) in these inwardly grown  $\rm Cr_2O_3$  intrusions suggest oxidation of the interfacial voids which formed due to the oxidation-induced Cr-loss and the following vacancy injection.

Comparison of Crofer 22 APU and Crofer 22 H reveals another interesting microstructural feature of oxidation of these steels, i.e., internal oxidation. The internal oxidation zone (IOZ) in Crofer 22 APU (Fig. 5a) is visible and well-pronounced while the precipitation of

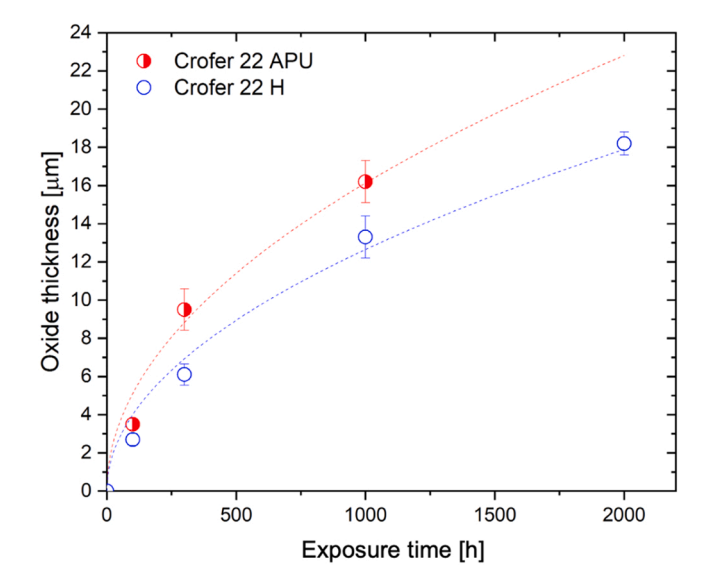


Fig. 3. Temporal evolution of oxide thickness on 0.2 mm thick foils of Crofer 22 APU and Crofer 22 H during air oxidation at 900  $^{\circ}$ C.

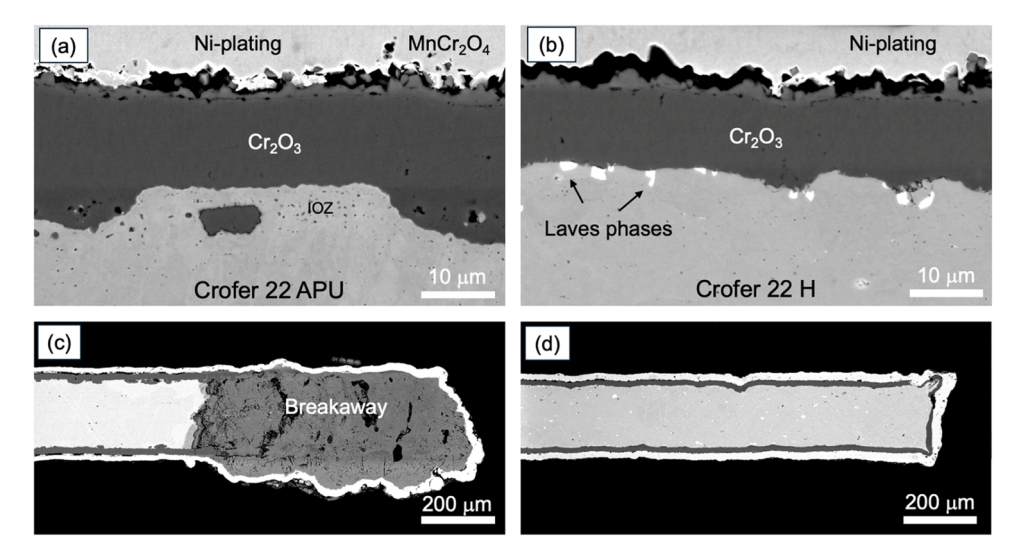


Fig. 2. BSE images of cross-sectioned 0.2 mm thick specimens of Crofer 22 APU (a,c) and Crofer 22 H after 1000 h air exposure at 900°C: oxide scales in the middles of the specimen (a,b) and specimen edges (c,d).

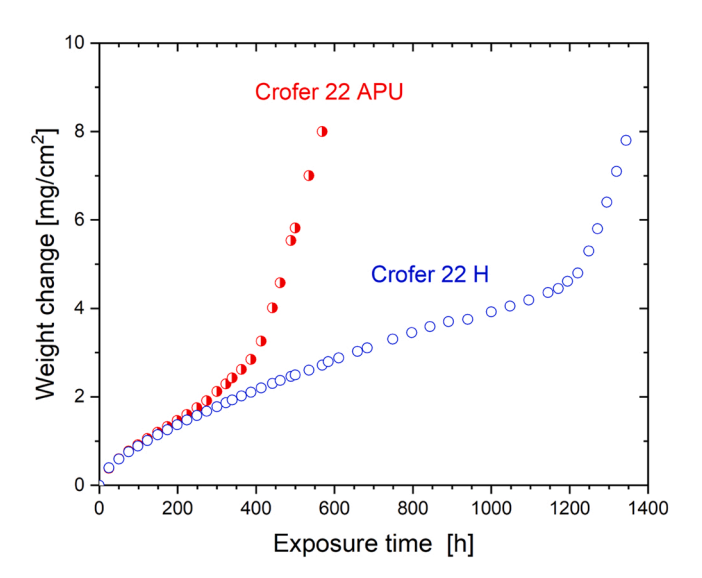


Fig. 4. Weight change for 0.3 mm thick foils of steel grades Crofer 22 APU and Crofer 22 H during discontinuous air oxidation for up to 1200 h at  $950^{\circ}$ C.

internal oxide ( ${\rm TiO_2}$ ) is not obvious in Crofer 22 H (Fig. 5a). The internal precipitates in Crofer 22 H tend to segregate to either alloy GBs or the rolling lines parallel to the surface. A detailed analysis of multiple SEM images revealed that the precipitation depth in both steels is similar although the precipitation patterns are different, presumably due to the differences in the composition of the steels and, hence, different nucleation kinetics.

#### 3.3. Oxidation at 1000 °C

Fig. 6 shows weight change for 0.3 mm thick foils of Crofer 22 APU and Crofer 22 H during air exposure at  $1000\,^{\circ}$ C. In contrast to the  $900\,^{\circ}$ C exposure (Fig. 1), both steel grades demonstrate a breakaway behaviour within  $1000\,h$ . Crofer 22 APU runs into accelerated oxidation after  $100\,h$  while Crofer 22 H remains in a protective oxidation mode for up to  $700\,h$ .

Fig. 7a-d presents BSE SEM images of oxide scales grown on Crofer 22 APU and Crofer 22 H foils after 300 h and 1000 h air oxidation at 1000 °C. The oxide scale grown on Crofer 22 APU is slightly thicker than that on Crofer 22 H, however the difference is smaller compared to 900 °C (Fig. 2). The oxide thickness evolution at 1000 °C is summarized in Fig. 8. Both Crofer 22 APU and Crofer 22 H suffer from breakaway oxidation at the edges of the foil specimens (Fig. 7e,f) after 1000 h in air at 1000 °C (compare with 900 °C in Fig. 2c). The extent of lateral damage is higher for Crofer 22 APU (1.5 mm from the edge) compared to Crofer 22 H (1.0 mm).

The main difference between the exposures at 900–950 °C and 1000 °C is a layer that appears brighter in the BSE images underneath the oxide scale in Crofer 22 APU after 300 h oxidation at 1000 °C (Fig. 7a,c). This layer is not observed underneath the  $\rm Cr_2O_3$  scale at 950 °C (Fig. 5a), however a bright-contrast layer is present underneath the non-protective oxide at the edge of the specimen (Fig. 5c). This layer hereafter will be termed AAZ, austenitization affected zone.

#### 3.4. Oxidation at 1050 °C

Fig. 9 shows oxidation kinetics curves for 0.3 mm thick foils of Crofer 22 APU and Crofer 22 H during air exposure at 1050 °C. The temperature is extreme for both Crofer 22 APU and Crofer 22 H which rapidly degrade into breakaway oxidation mode within 300 h (first signs of oxidation of the edges for Crofer 22 H) and only 50 h for Crofer 22 APU.

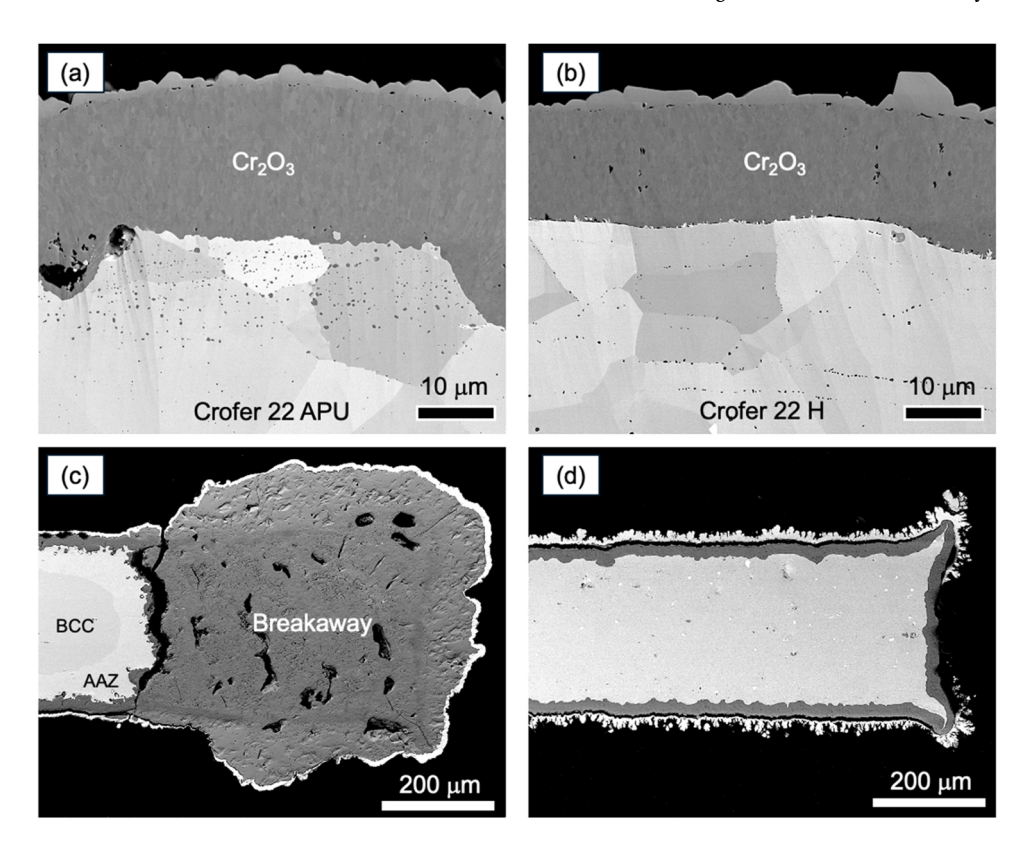


Fig. 5. BSE images of cross-sectioned 0.3 mm thick specimens of Crofer 22 APU (a,c) and Crofer 22 H after 1000 h of discontinuous exposure in air at 950°C: oxide scales in the middles of the specimen (a,b) and specimen edges (c,d). Symbol AAZ in fig. (c) denotes austenitization affected zone formed underneath the breakaway area in Crofer 22 APU.

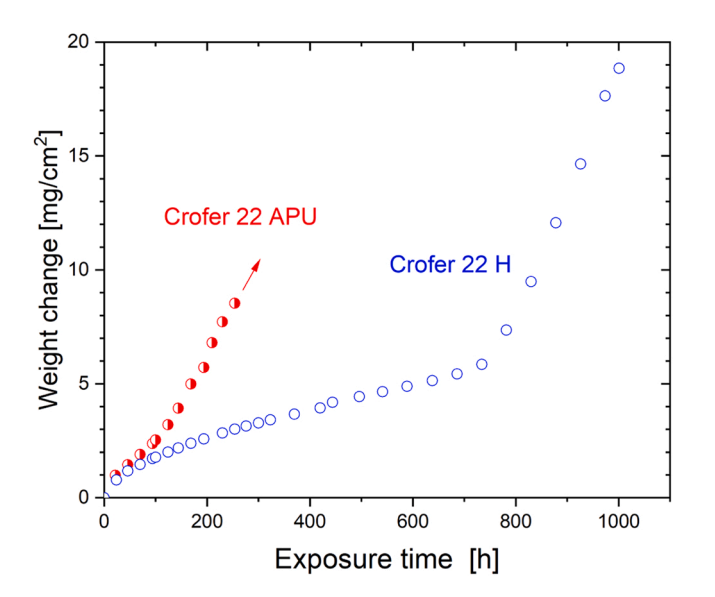


Fig. 6. Weight change for 0.3 mm thick foils of Crofer 22 APU and Crofer 22 H during discontinuous air oxidation for up to 1000 h at  $1000^{\circ}$ C.

Fig. 10 demonstrates BSE SEM images of the oxide scales formed on Crofer 22 APU after 200 h air exposures at 1050  $^{\circ}$ C. Similar to 1000  $^{\circ}$ C, a continuous 50  $\mu m$  thick bright-contrast AAZ formed immediately

underneath the  $Cr_2O_3$  scale (Fig. 10a). The specimen edge shown in Fig. 10b is heavily corroded and reveals a broad (700  $\mu$ m) zone of full transformation of the alloy from BCC to FCC (see also inset in Fig. 10c).

Fig. 11 shows BSE images of the oxide scales formed on the Crofer 22 H foil after 500 h air exposures at 1050 °C. Big cavities are visible at the oxide-metal interface indicating a strong vacancy injection due to Cr-loss and the following condensation of the vacancies. The specimen edge shows signs of internal and breakaway oxidation, but no  $\alpha\text{-to-}\gamma$  transformation is observed in Crofer 22 H in the BSE SEM image in contrast to Crofer 22 APU in (Fig. 10c). Austenitization of Crofer 22 H at 1050 °C was revealed by etching the cross-sections with KALLING 1. Optical micrographs shown in Fig. 12 demonstrate the fine-grained microstructure of the AAZ underneath the  $\text{Cr}_2\text{O}_3$  scale in Crofer 22 APU (Fig. 12a, compare with BSE SEM image in Fig. 10a) as well as the presence of AAZ in Crofer 22 H in the vicinity of the IOZ and the breakaway area at the foil edge (Fig. 12b, compare with BSE SEM image in Fig. 11b). Austenitization is thereby confirmed also for Crofer 22 H.

# 3.5. Cr depletion dynamics

Fig. 13a shows Cr-concentration profiles measured with EDX in the oxidized 0.2 mm thick foils of Crofer 22 APU (full symbols) and Crofer 22 H (empty symbols) exposed in air for up to 2000 h at 900 °C. After 100 h at 900 °C, the Cr depletion profiles are close to reaching the midplane of the foil. The calculated Cr depletion distance, approximated as  $\zeta = \sqrt{4Dt}$ , is 110 µm after 100 h at 900 °C being close to the half-

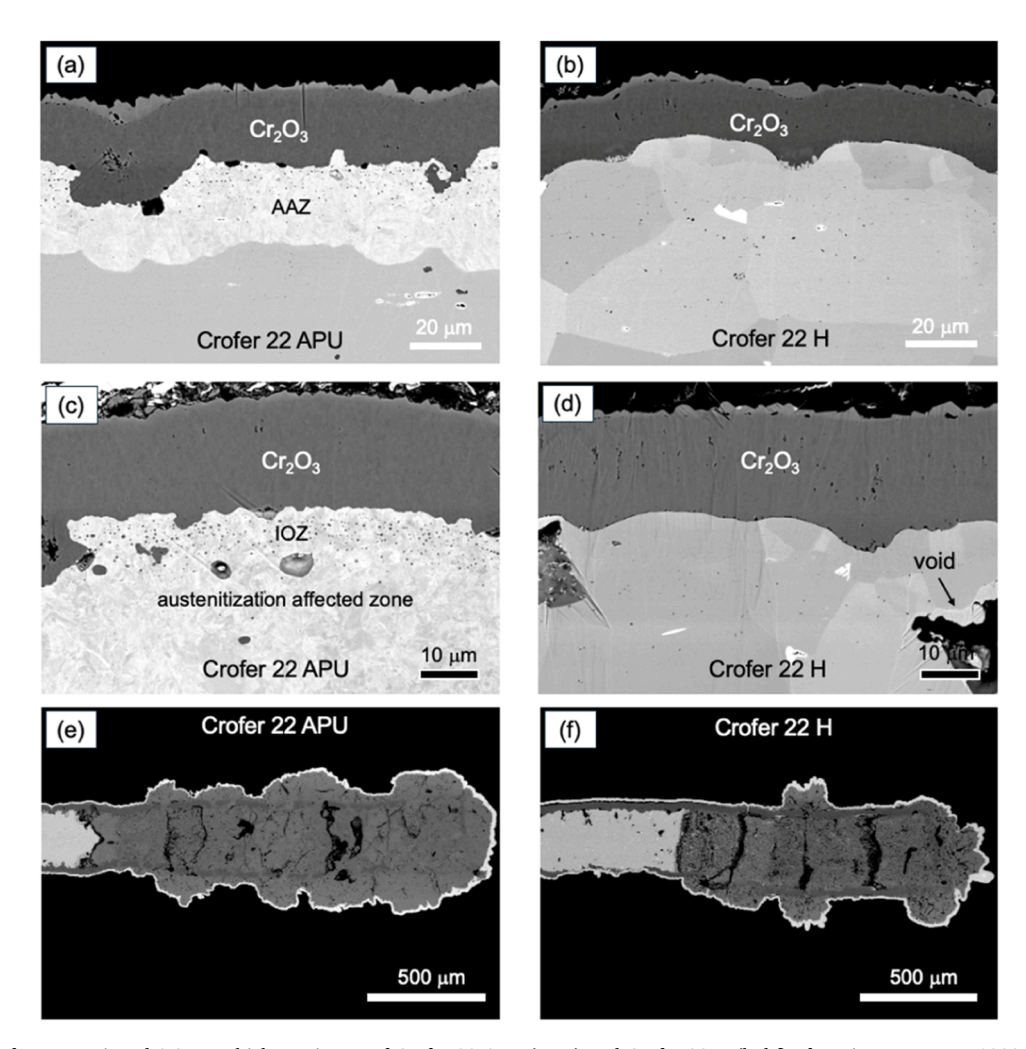


Fig. 7. BSE images of cross-sectioned 0.3 mm thick specimens of Crofer 22 APU (a,c,e) and Crofer 22 H (b,d,f) after air exposure at 1000°C: oxide scales in the middles of the specimen after 300 h (a,b), 1000 h (c,d) and specimen edges after 1000 h (e,f).

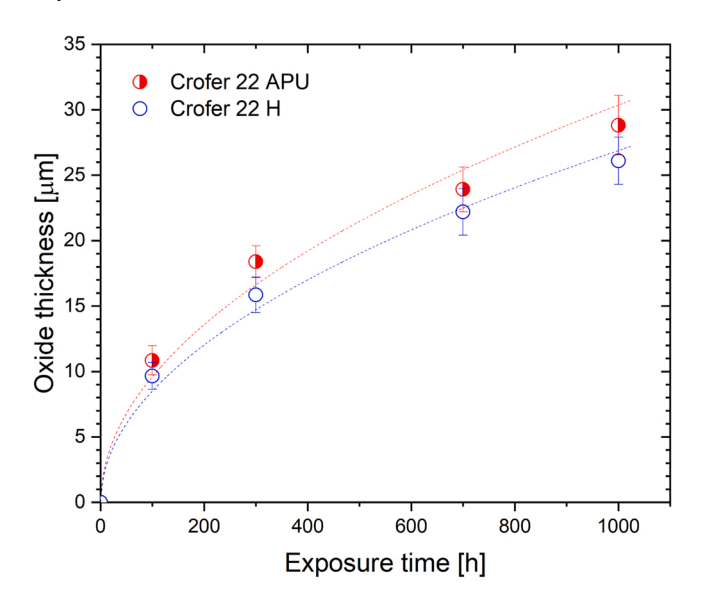
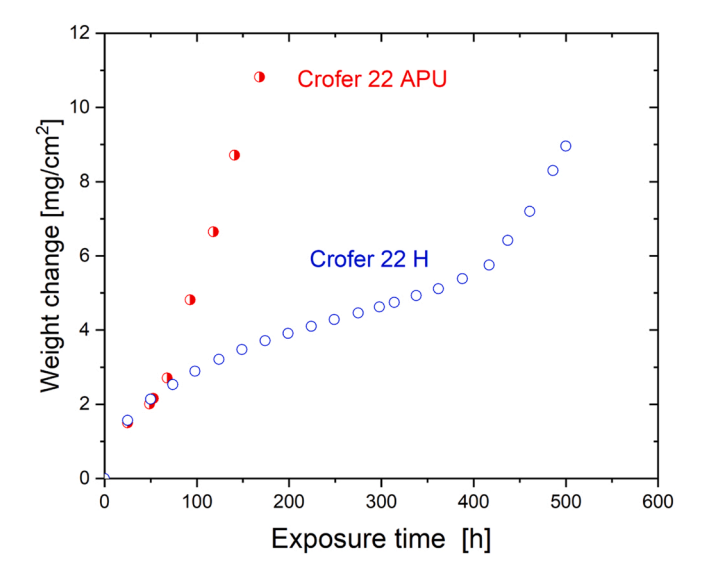


Fig. 8. Temporal evolution of oxide thickness on 0.3 mm thick foils of Crofer 22 APU and Crofer 22 H during air oxidation for up to  $1000\,h$  at  $1000^\circ C$ .



**Fig. 9.** Weight change for 0.3 mm thick foils of steel grades Crofer 22 APU and Crofer 22 H during discontinuous air oxidation for up to 1200 h at 1050°C.

thickness of the foil. Thus, the experimental Cr-interface concentrations can still be reasonably predicted by Eq. S4 (see Data supplement and Table 2). The calculated depletion by 3 wt% agrees well with the measured Cr depletion values (see profiles after 100 h in Fig. 13a). This implies that Cr depletion profiles in ferritic steels are not necessarily flat and uniform in the beginning (see also [24]). However, the Cr profiles flatten out as the oxidation proceeds. After the depletion fronts meet at the mid-plane of the foil, the Cr gradient across the specimen gradually decreases and virtually vanishes after 2000 h in the Crofer 22 H foil Fig. 13a.

Fig. 13b shows a temporal evolution of the Cr-concentration at the oxide-metal interface in 0.2 mm thick foils of Crofer 22 APU and Crofer 22 H during air exposure at 900 °C measured by EDS and calculated using Eq. S7. The WD model accurately predicts the Cr depletion kinetics in both Crofer 22 APU and Crofer 22 H. As can be expected from the slightly faster oxidation kinetics of Crofer 22 APU compared to Crofer 22 H (Fig. 8), Crofer 22 APU is faster depleted of Cr. However, this effect is not strong. After 2000 h, the WD model predicts 1,5 wt% difference between Crofer 22 APU and Crofer 22 H. The remaining Cr-interface concentration in Crofer 22 APU after the onset of breakaway at 700 h is 17 wt%.

The situation is fundamentally different at 1000  $^{\circ}$ C (Fig. 14a). First, the depletion fronts reached the mid-plane before the first sampling point (100 h) and the Cr profiles are already virtually flat after 100 h. Second, the Cr profiles in Crofer 22 APU become steeper in the near-surface region after 300 h. The Cr profiles in Crofer 22 H remain flat up to 1000 h at 1000  $^{\circ}$ C. This time, the WD model correctly predicts the temporal evolution of the Cr-interface concentration only for Crofer 22 H (Fig. 14b). In contrast to 900  $^{\circ}$ C, the difference in Cr-concentration between Crofer 22 APU Crofer 22 H after 1000 h at 1000  $^{\circ}$ C amounts to 9 wt%.

# 3.6. Austenitization in Crofer 22 APU

The steeper part in the Cr depletion profiles in Crofer 22 APU (Fig. 14a) is due to the FCC layer formed in the immediate vicinity of the  $\rm Cr_2O_3$  scale (Fig. 7a). At 1000°C, the Cr diffusion in the FCC lattice by an order of magnitude slower than in BCC [31], which is expected to decrease the Cr-interface concentration. The austenitization affected zone (AAZ) is not observed at 950 °C (Fig. 5a) but it forms at the edge of the foil (Fig. 5b) where Cr-depletion is more intense.

The microstructural evolution, i.e., the growth of AAZ in the Crofer 22 APU foil during the exposure at 1000  $^{\circ}$ C, is visually summarized in Fig. 15 along with the corresponding micrographs for Crofer 22 H in which no austenitization occurred. Crofer 22 H (upper row) continues to have a BCC matrix for up to 1000 h of exposure and reveals a gradual grain coarsening and formation of voids. The grains in Crofer 22 APU

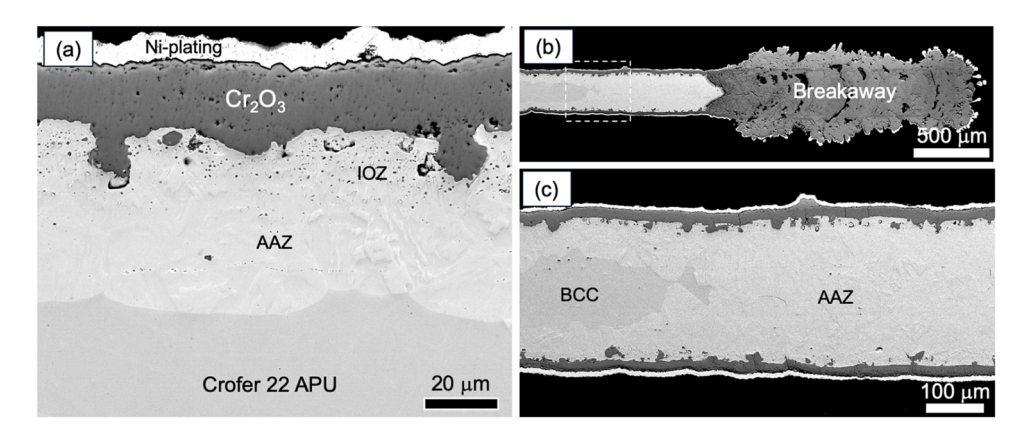


Fig. 10. BSE images of cross-sectioned 0.3 mm thick specimens of Crofer 22 APU after 200 h of discontinuous exposure in air at 1050°C: (a) oxide scale in the middles of the specimen, (b) specimen edge, and (c) zone of complete BCC to FCC transformation. AAZ marks austenitization affected zone.

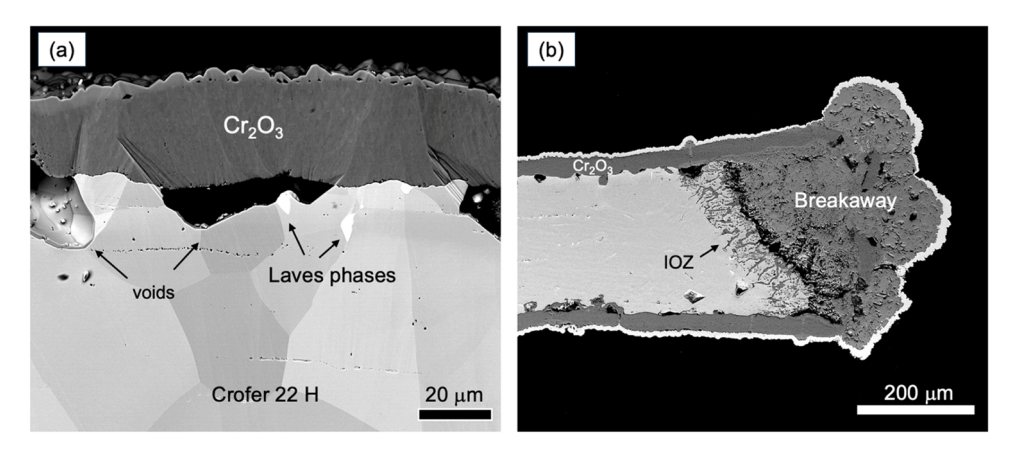


Fig. 11. BSE images of cross-sectioned 0.3 mm thick specimens of Crofer 22 H after 500 h of discontinuous exposure in air at 1050°C: (a) oxide scale in the middles of the specimen and (b) specimen edge.

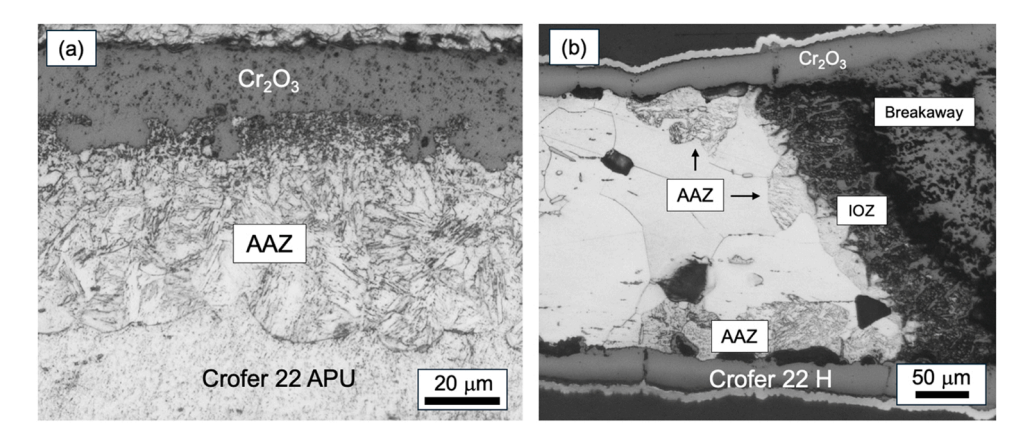


Fig. 12. Optical micrographs of cross-sectioned specimens of (a) Crofer 22 APU after 200 h and (b) Crofer 22 H after 500 h air oxidation at 1050 °C. Etched with KALLING 1. AAZ marks austenitization affected zone.

coarsened rapidly after 100 h. A bright-contrasts layer (Fig. 7a,c) can be observed after 300 h oxidation. After 1000 h of oxidation, the initial BCC phase in Crofer 22 APU is almost completely consumed by AAZ. At 1050  $^{\circ}$ C, the AAZ fully consumed the ferritic matrix in the specimen edge Fig. 10. It is obvious that AAZ appears primarily in Crofer 22 APU and is susceptible to Cr-depletion which is more intense at the edges/corner of the specimens due to a higher surface-to-volume ratio. However, the austenitization has also been detected in Crofer 22 H (Fig. 12b) albeit in the extreme conditions of exposure at 1050  $^{\circ}$ C.

# 4. Discussion

# 4.1. Criteria of chemical failure

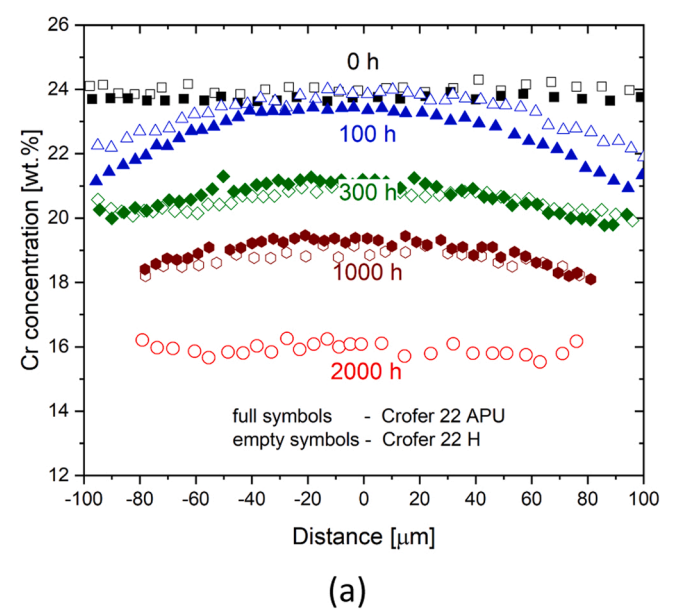
The accuracy of the lifetime prediction tools critically depends on two input parameters: i) kinetic data ( $k_c$  and D) and ii) the critical concentration  $N_B^{crit}$ . While  $k_c$  and D are directly measurable, well tabulated and can be re-measured for every specific case, determination of  $N_B^{crit}$  is not always straightforward. According to the classical theory of selective oxidation [32], oxidation of the base metal A (with A = Fe or Ni) is possible only if the oxygen potential at the oxide-metal interface set by the equilibrium  $BO_v/B$  (Cr<sub>2</sub>O<sub>3</sub>/Cr in the present study) increases to the level of that for  $AO_{\varnothing}/A$  (FeO/Fe), see also [33] or [34]. In practical terms, this implies that  $N_B^{rit} = 0$ . Indeed, zero concentration of Al is commonly adopted for lifetime calculations for thin foils of FeCrAl using the MB model [12], with corrections being made for sub-parabolic oxidation kinetics.

The original publications [13,14] introducing the WD model also

postulated  $N_{Cr}^{crit} = 0$  as an ultimate end-of-life criterion. However, Cowen and Webster [14] experimentally measured 7-16 wt% of remaining Cr in the foil specimens (5-10 µm thick) of 25Cr20Ni austenitic steel exposed to CO2 at 750 °C removed from the exposure prior breakaway oxidation. Evans et al. experimentally demonstrated in numerous studies [16,34,35] describing Cr-depletion in foils of 20Cr25Ni austenitic steels at 900-950 °C that breakaway oxidation occurred while the foils still contained 8 (at the surface) to 16 (in the middle) wt% Cr. In these studies, as well as in the later ones [15], WD accurately predicted the Cr depletion profiles. Finally, an averaged value of  $N_{Cr}^{crit} = 0.11$ (10 wt%) Cr was reported for a ferritic steel grade Crofer 22 APU at 900 °C [19] and a porous model alloy Fe22Cr at 750 °C [22,23]. The afore-mentioned experimental evidence can be summarized as follows: in contrast to alumina-formers, austenitic and ferritic steels forming chromia scales suffer from breakaway oxidation long before the available Cr reservoir is completely exhausted ( $N_{Cr}^{crit} = 0$ ).

Despite the obvious similarities, the mechanisms explaining this phenomenon are different for austenitic (FCC) and ferritic (BCC) alloys. The case of austenitic steels was thoroughly elaborated by Evans et. al. in [34] who differentiated between two separate phenomena: i) intrinsic chemical failure (InCF) and ii) mechanically induced chemical failure (MICF). The concept of InCF originates from a thermodynamic analysis showing that Cr needs to be depleted virtually to zero for iron to start to oxidize. MICF occurs in the event of oxide spallation when the Cr-depleted subsurface alloy is unable to re-grow  $Cr_2O_3$ .

*MICF* is easy to interpret based on the classical Wagnerian diffusion analysis [32,36] (see Data supplement for more details). For instance, at 900  $^{\circ}$ C when an austenitic alloy is depleted to 8–10 wt% at the



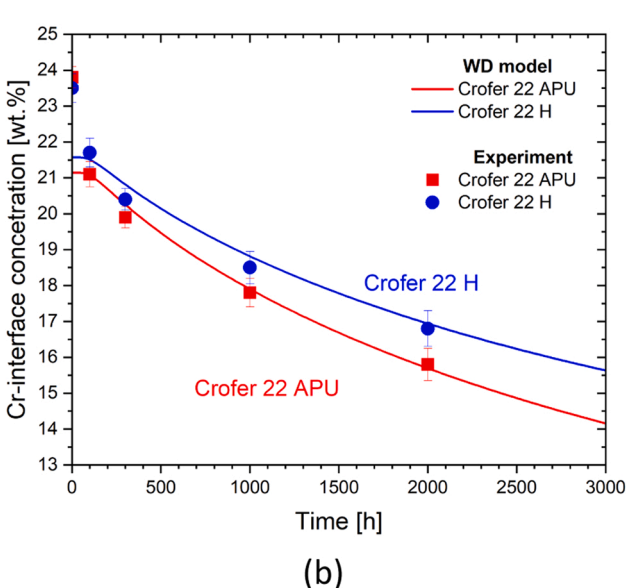


Fig. 13. Cr-depletion profiles (a) and temporal evolution of Cr-interface concentration (b) in 0.2 mm thick foils of Crofer 22 APU and Crofer 22 H after air oxidation at 900  $^{\circ}\text{C}.$  Cr concentrations were measured with EDX in cross-sectioned specimens after up to 2000 h.

oxide-metal interface and the depleted alloy is exposed to the oxidizing atmosphere (e.g. after oxide spallation), neither Wagnerian criterion 1 (Eq. S9) nor criterion 2 (Eq. S10) are fulfilled (see Table S1). The area of oxide spallation will suffer from breakaway while the area covered with  $\rm Cr_2O_3$  will remain protective. Therefore, the main reason for the high remnant Cr content in post-breakaway austenitic specimens is slow Cr diffusion in FCC resulting in the intense Cr surface depletion and increasing the risk of  $\it MICF$  due to e.g. oxide spallation or cracking.

The situation with ferrites is different because Cr diffusion is rapid and the second Wagnerian criterium is fulfilled almost throughout the entire compositional range of Cr virtually to zero. Despite rapid diffusion of Cr in BCC, ferritic steels are also reported to fail after being depleted to  $8{\text -}10$  wt%. This may have two explanations.

First, a Cr depleted ferritic FeCr alloys will face the same re-healing problem once exposed to oxidizing gas after oxide spallation/cracking. The supply criterion (Eq. \$10) is fulfilled for such an alloy at \$00-1000 °C. However, this Cr depleted alloy will be close to the formation

criterion (Eq. S9), which is estimated to vary between 8 and 10 wt% for FeCr at 800–1000 °C (see for more details in [25]). In other words, *MICF* is also relevant for ferritic steels once the Cr level drops below 10 wt%.

In the present study, the Crofer 22 APU specimens ran into break-away oxidation while the foils still contained 18–21 wt% in the middle of the specimen. This is hard to explain with *MICF* because with the measured interface concentration of 17 wt%, both Wagnerian criteria (Eq. S9 and S10) were fulfilled.

The second reason of breakaway in ferritic steels at relatively high Cr concentration is the  $\alpha\text{-to-}\gamma$  phase transformation occurring above  $850\,^{\circ}\text{C}$  in ferritic steels unless they are alloyed with ferrite-stabilizing elements [24]. This phenomenon will be discussed in detail in the following sections. To summarize, premature breakaway oxidation of FeCr-base alloys occurs due to two reasons:

- i) inability to re-grow  $Cr_2O_3$  once depleted to 8–10 wt% at the oxidemetal interface and exposed to oxidation via mechanical failure (valid for FCC and BCC alloys in the entire temperature range)
- ii) Austenitization of Fe-Cr due to Cr depletion (valid for BCC alloys approximately above 850  $^{\circ}\text{C}$ ).

#### 4.2. Oxidation kinetics and breakaway

The steel grade Crofer 22 H was developed based on the concept of Crofer 22 APU via further alloying with W and Nb to simultaneously achieve a solution strengthening effect as well as precipitation hardening by Laves-phase in combination with a higher tolerance for Si [37]. A higher creep resistance of Crofer 22 H with respect to Crofer 22 APU [28] was found to have a measurable effect on the oxidation kinetics. Oxidation rate of Crofer 22 APU was demonstrated to be strongly thickness dependent, the oxidation rate increasing with decreasing specimen thickness [21,38]. This effect is related to a plastic deformation of the alloy substrate and is much weaker for Crofer 22 H [20] and has never been reported for strengthened Ni-base alloys. In available literature, Crofer 22 APU is systematically reported to oxidize slightly faster than Crofer 22 H for a given specimen thickness [20].

This effect was reproduced in the present work (Fig. 1 and Fig. 3). Interestingly, this difference between Crofer 22 APU and Crofer 22 H substantially decreased at  $1000\,^{\circ}\text{C}$  (Fig. 8). The Laves-phase is less stable above  $1000\,^{\circ}\text{C}$  and is not a strengthening factor anymore, e.g., not preventing the alloy grains from coarsening (Fig. 15) and loss of creep resistance. It was demonstrated in [20] that ageing of Crofer 22 H for 500 h at 900  $^{\circ}\text{C}$ , coarsening the Laves-phases precipitates at the GBs, resulted in a higher creep and oxidation rates of aged Crofer 22 H. The oxidation rates of aged Crofer 22 H were close to those of Crofer 22 APU.

It is clear thus that Crofer 22 APU oxidizes slightly faster than Crofer 22 H (applies to specimens with a given thickness), which results in somewhat faster Cr-depletion (Fig. 13) at 900 °C. However, this effect is rather limited, e.g., 1 wt% after 1000 h at 900 °C. Such a small difference is unlikely to prematurely provoke breakaway oxidation, especially because the Cr-interface concentration in Crofer 22 APU amounted to 18 wt% at the onset of breakaway after 700 h of exposure. The faster oxidation kinetics of Crofer 22 APU is hardly the reason for its poor performance at 900 °C with respect to Crofer 22 H.

Another important difference between Crofer 22 APU and Crofer 22 H is the chemical composition (Table 1). Crofer 22 H is additionally alloyed with ferrite stabilizing elements such as W, Nb and Si. These alloying additions are the key factor preventing Crofer 22 H from austenitization due to Cr-depletion during oxidation.

# 4.3. Austenitization triggering breakaway

Fig. 16 demonstrates a fragment of the binary Fe-Cr phase diagram highlighting the austenite loop. Crofer 22 APU can be approximated as a binary Fe-23Cr alloy while a separate calculation was performed for Crofer 22 H including W, Nb, and Si using Thermo-Calc and TCFE6

**Table 2** Examples of calculating  $k_c/D$  values for different alloy systems based on literature data and experimentally measured  $k_c$  values in the present study.  $k_c$  values are calculated based on experimental oxide thickness measurements and D values for ferritic Fe-Cr are taken from [31]. The values for  $N_B^0 - N_B^{\text{int}}$  are calculated using Eq. S4. Literature data for Fe-Cr-Al are taken from [6], Ni-Cr [13], and Fe-Cr-Ni [15].

Alloy system	lattice	Oxide	T [°C]	$k_c [\mathrm{m}^2 \mathrm{s}^{-1}]$	$D [m^2 s^{-1}]$	$k_c/D$	$N_B^0-N_B^{int}$
Literature data							
Fe-Cr-Al	BCC	$Al_2O_3$	1200	$1  imes 10^{-17}$	$5 imes10^{-13}$	$2  imes 10^{-5}$	0006
Fe-Cr	BCC	$Cr_2O_3$	900	$5,6  imes 10^{-18}$	$9  imes 10^{-15}$	$6  imes 10^{-4}$	0031
Ni-Cr	FCC	$Cr_2O_3$	1200	$1 imes10^{-15}$	$5  imes 10^{-14}$	$2  imes 10^{-2}$	0177
Fe-Cr-Ni	FCC	$Cr_2O_3$	1013	$1.5\times10^{-17}$	$1.5\times10^{-15}$	$1  imes 10^{-2}$	0125
This work							
				Exp.	from [31]		
Crofer 22 APU	BCC	$Cr_2O_3$	900	$6.8 \times 10^{-18}$	$9 \times 10^{-15}$	$7.6 \times 10^{-4}$	0035
Crofer 22 H	BCC	$Cr_2O_3$	900	$5,0  imes 10^{-18}$	$9  imes 10^{-15}$	$5,6 \times 10^{-4}$	0030
Crofer 22 APU	BCC	$Cr_2O_3$	950	$1,3 \times 10^{-17}$	$1,6  imes 10^{-14}$	$8.1  imes 10^{-4}$	0035
Crofer 22 H	BCC	$Cr_2O_3$	950	$1,3 \times 10^{-17}$	$1,6 \times 10^{-14}$	$8,1 \times 10^{-4}$	0035
Crofer 22 APU	BCC	$Cr_2O_3$	1000	$2,8  imes 10^{-17}$	$3,6 \times 10^{-14}$	$7.8 \times 10^{-4}$	0035
Crofer 22 H	BCC	$Cr_2O_3$	1000	$2,6 \times 10^{-17}$	$3,6 \times 10^{-14}$	$7,2 \times 10^{-4}$	0033
Crofer 22 APU	BCC	$Cr_2O_3$	1050	$9,0 \times 10^{-17}$	$9,0 \times 10^{-14}$	$1,2 \times 10^{-3}$	0,04
Crofer 22 H	BCC	$Cr_2O_3$	1050	$9.0 \times 10^{-17}$	$9.0 \times 10^{-14}$	$1,\!2\times10^{-3}$	0,04

database [39]. A T-Cr section from this multicomponent calculation is superimposed on the binary phase diagram in Fig. 16 which illustrates the interplay between temperature, Cr-depletion, and the  $\alpha\text{-to-}\gamma$  phase transformation during oxidation of thin Crofer 22 APU and Crofer 22 H foils. A detailed description of how the phase diagram for Crofer 22 H was constructed is given in Data supplement.

Fig. 16 allows a quantitative estimation of the austenitization boundaries (temperature and concentration) for Crofer 22 APU and Crofer 22 H at 900 and 1000 °C. The initial composition of both Crofer 22 APU and Crofer 22 H (approximately 23 wt% Cr) corresponds to ferrite (BCC) at 900 and 1000 °C. As oxidation proceeds, the Cr concentration in the foils decreases with time due to Cr consumption by oxidation (Fig. 13b). According to Fig. 16, the lowest temperature of the austenite loop for Crofer APU is at 850 °C and 6.5 wt% Cr. Alloying Fe-Cr with W, Nb and Si squeezes the austenite loop and shifts this point to 930 °C and 5.5 wt% Cr. The critical Cr concentration can also be established for a given temperature. For the unalloyed binary Fe-Cr system (Crofer 22 APU), the α-to-γ transition occurs at 12.7 wt% Cr at 900  $^{\circ}\text{C}$  and 14.2 wt% Cr at 1000  $^{\circ}\text{C}.$  In Crofer 22 H, the austenite loop shrinks so much that no austenitization can occur at 900 °C. At 1000 °C, austenitization is possible and will occur at 9.0 wt% Cr, i.e., at a 5 % lower Cr concentration level compared to Crofer 22 APU.

Austenitization has been recently demonstrated to be the primary reason of breakaway oxidation in ferritic FeCr-base model alloys at 900 °C [24,25]. The  $\alpha$ -to- $\gamma$  transformation is most likely to occur at sharp edges of a specimen where Cr depletion is the most intense due to a higher surface-to-volume ratio [11,40]. In the present study as well as in the other similar studies [19,41], breakaway oxidation initiates at the specimen edges (Fig. 2c, Fig. 5c, and Fig. 7e,f). After 1000 h at 900°C, the Cr-interface concentration in the Crofer 22 APU specimens is 17.8  $\pm$  0.3 wt% (see Fig. 13a) which is far from the austenite loop. At the same time, the Crofer 22 APU specimens have already gone into breakaway oxidation (Fig. 1) at the edges. The Crofer 22 H foils were protective for up to 2000 h at 900 °C and were depleted to 16.9  $\pm$  0.3 wt % of Cr at the oxide-metal interface.

The thermodynamic analysis in Fig. 16 correctly predicts the  $\alpha\text{-to-}\gamma$  transformation for Crofer 22 APU and its absence for Crofer 22 H (resulting in protective behaviour) at 900 °C. Furthermore, the phase diagram in Fig. 16 accurately predicts austenitization for both steel grades above 950 °C.

It is important to mention that austenitization is an important step and prerequisite in the mechanism but not necessarily the final one. The key event is the critical depletion of Cr, i.e., the drop of Cr concentration to virtually zero. For instance, the  $Cr_2O_3$  scale on Crofer 22 APU at 1000 °C keeps growing upon the FCC layer (Fig. 15) while the interface concentration of Cr is approx. 9 wt% after 1000 h (Fig. 14a). At the same

time, breakaway oxidation significantly progressed at the corners/edges of the Crofer 22 APU foil specimen (Fig. 7e).

Therefore, an even more important factor of transition from austenitization to breakaway oxidation is specimen geometry. The  $\rm Cr_2O_3$  scale can continue to grow on a flat layer of austenite but not on the corner/edge where Cr-depletion is much more intense. When the austenite grains become depleted of Cr from three/two surfaces, the Cr-interface concentration rapidly drops to the critical level resulting in breakaway oxidation.

This effect is also valid for other systems. Austenitization occurring in the Fe-Cr system is the most likely reason for the immediate transition of FeCrAl alloys into breakaway oxidation once their Al reservoir is exhausted. After Al is completely consumed, the alloy virtually transforms into Fe-20Cr which potentially could continue to perform in a relatively protective mode as a chromia-former smoothing the transition from protective to catastrophic oxidation as demonstrated e.g. for thin foils of NiCrAl-base alloy Haynes 214 at 1100 and 1200 °C [42,43]. However, this is unlikely for a binary Fe-20Cr because its ferritic microstructure is not anymore stabilized by Al consumed by oxide scaling. At 1100–1200 °C, Fe-20Cr will immediately undergo the  $\alpha$ -to- $\gamma$  transformation (see the  $\gamma$ -loop in Fig. 16) at the corners/edges as described in [24] and suffer from rapid oxidation of iron.

# 4.4. Implications for lifetime modelling

In this section, the available lifetime prediction models will be applied to the case of Crofer 22 APU and Crofer 22 H critically assessing the input parameter  $N_{Cr}^{crit}$  while bearing in mind a risk of austenitization in the Fe-Cr system at 900 °C and above. The values of  $t_B$  for Crofer 22 APU and Crofer 22 H were calculated using the mass-balance model (MB) [19] given by

$$t_{B} = l^{2} \frac{\left(N_{B}^{0} - N_{B}^{crit}\right)^{2}}{2k_{c}} \tag{1}$$

and reduced Whittle depletion (RW) [18] model based on Whittle depletion model (WD) [13] and given by the following expression

$$t_B = l^2 \left[ \frac{\left( N_B^0 - N_B^{crit} \right)^2}{2k_c} - \frac{\alpha}{D} \right]. \tag{2}$$

Here  $N_B^0$  is the initial concentration of Cr in the steel,  $N_B^{crit}$  critical concentration of Cr at which protective oxidation can no longer be sustained, l half-thickness of the sheet specimen in m,  $k_c$  parabolic rate of oxidation expressed in terms of metal recession in  $m^2s^{-1}$ , D interdiffusion coefficient of Cr in the steels in  $m^2s^{-1}$ ,  $\alpha$  dimensionless universal constant equal 0.37. The detailed derivation of both models is given in

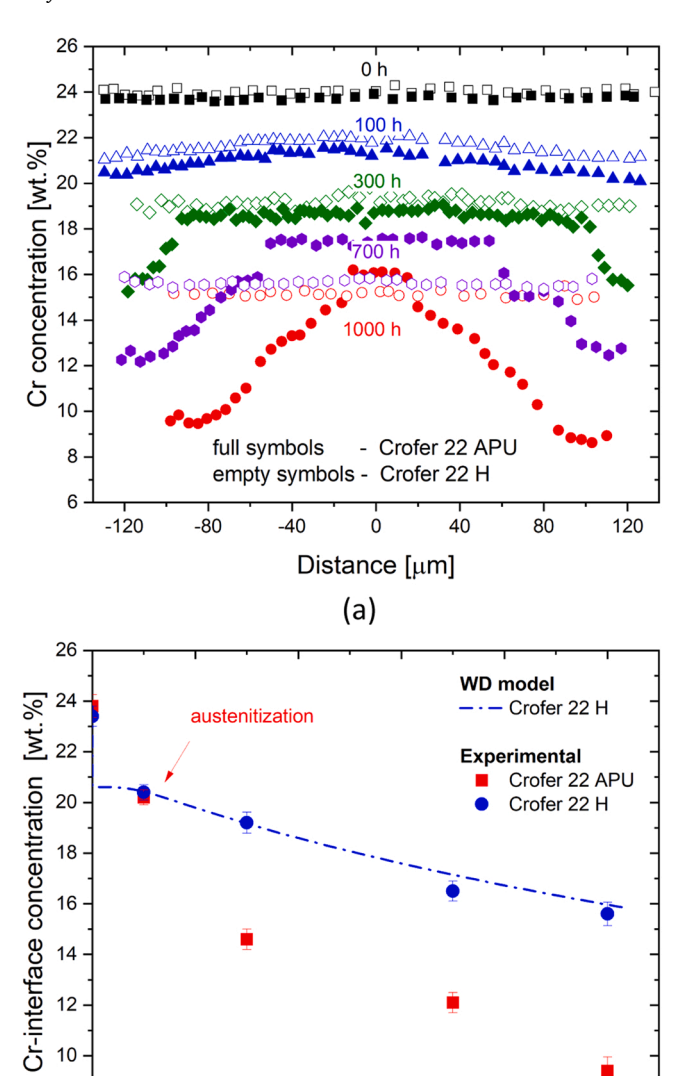


**Fig. 14.** Cr-depletion profiles (a) and temporal evolution of Cr-interface concentration (b) in 0.3 mm thick foils of Crofer 22 APU and Crofer 22 H after air oxidation at  $1000\,^{\circ}$ C. Cr concentrations were measured with EDX in cross-sectioned specimens after  $100,\,300,\,700,\,$  and  $1000\,$ h.

600

Time [h]

(b)

800

1000

400

200

#### Data supplement.

8

0

The kinetic parameters for Eqs. (1) and (2) from Table 2 are summarized in Table 3. A classical failure criterion  $N_{Cr}^{crit}=0.11$  or 10 wt% Cr was adopted for this baseline calculation. It is worth noting that the  $t_B$  values computed using both models are close, i.e., the RW values are no more than 8 % lower that the MB values. The latter implies that the  $k_c/D$  ratio is sufficiently low ( $<1\times10^{-2}$ , see also Table 2) and the Cr depletion profiles are acceptably uniform so that both models are reasonably applicable.

However, the  $t_B$  values predicted by both models significantly exceed the experimental values by a factor ranging from 2.5 to 15 (Table 3). The experimentally measured residual Cr-interface concentrations,  $N_{Cr}^{int}$ , (see Table 3) in the post-breakaway foils varied from 17 to 21 wt%, which is very far from  $N_{Cr}^{int}$  defined by either *MICF* [34] or the formation criterion of Wagner (Eq. S9) [36].

Such a strong overprediction of  $t_B$  in the present case has two rea-

sons: i) geometrical constraints at the edges and corners of the tested coupons and ii) α-to-γ transformation occurring above 850 °C (Crofer 22 APU) and 930 °C (Crofer 22 H) in the Cr-depleted corners of the specimens. The AC model (austenitization of corners) proposed here addresses these problems and results in accurate lifetime predictions presented in Table 3. It is well-known that breakaway oxidation tends to initiate at sharp corners/edges due to a higher surface-to-volume ration at corners, edges, sharp tips causing a simultaneous and faster Crdepletion of the underlying volume through multiple surfaces (two sides for an edge and three sides for a tip-point of the specimen corner) [11,40]. This geometrically accelerated Cr-removal can be considered by introducing a geometrical factor,  $f_{\text{geo}}^{\ast},$  as e.g. in [10] into Eq. 2. Another amendment to make in Eq. 2 is the substitution of  $N_R^{crit}$  by  $N_R^{aust}$ , the concentration of Cr at the  $\gamma/\alpha$ -boundary at a given temperature determined from the phase diagram in Fig. 16. This substitution is required to make the failure criterion more realistic under the assumption that austenitization of the specimen corner is the main trigger of breakaway oxidation. Once these two considerations are adopted, Eq. 2 corrected for austenitization of the specimen corners becomes:

$$t_B = l^2 \left[ \frac{\left( N_B^0 - N_B^{aust} \right)^2}{2f_{geo}^* k_c} - \frac{\alpha}{D} \right]. \tag{3}$$

here  $f_{\rm geo}^*$  is an integer for a given geometry, i.e.  $f_{\rm geo}^*=1$  for a plane surface,  $f_{\rm geo}^*=2$  for a 90° edge, and  $f_{\rm geo}^*=3$  for a corner tip of a cubic corner,  $N_B^{\rm cust}$  is the Cr concentration at which  $\alpha$ -BCC starts to transform into  $\gamma$ -FCC (Fig. 16). The values of  $t_B$  calculated using Eq. 3,  $f_{\rm geo}^*=3$ , and the corresponding  $N_B^{\rm cust}$  values are presented in (Table 3).

The geometry factor  $f_{geo}^*$  in Eq. 3 was additionally verified in an experiment with rounded coupons. The sharp corners of the foils were rounded by grinding. Fig. 17 compares weight gain curves for the 0.3 mm thick foils of Crofer 22 H exposed in air at 1000 °C (compare also with Fig. 6). The rounded specimens retained protectiveness after 1000 h while the rectangular coupons were significantly corroded at the corners/edges (Fig. 7f) after the same exposure time. The transition to breakaway oxidation of the rounded specimens occurred after 1050 h (Fig. 17).

Elimination of the corners mathematically corresponds to  $f_{geo}^*=2$  in Eq. 3, and thus some lifetime extension. The predicted lifetime increases from 707 h (rectangular specimen,  $f_{geo}^*=3$ ) to 1087 h (rounded specimen,  $f_{geo}^*=2$ ), respectively, in excellent agreement with experiment (Fig. 17).

The amended model considering austenitization of corners (the AC model) very accurately predicts  $t_B$  for all three cases. Clearly, the AC model is the most accurate one to describe a transition to breakaway oxidation involving the  $\alpha$ -to- $\gamma$  transformation in ferritic steels above 850 °C. In contrast to the other models (MB, WD, RD), the AC model employs a much more rigorously defined, metallurgy-based failure criterion. The AC model gives a quantitative estimation of a lifetime extension of Crofer 22 APU via alloying with ferrite stabilizers, e.g. W, Nb, Si to Crofer 22 H: at all test temperatures between 950, 1000 and 1050 °C, the lifetime extension factor,  $\frac{t_0^{Crofer22H}}{t_B^{Frofer22AFU}}$ , is close to 6. The experimentally measured lifetime extension factor varied from 5 to 7 (Table 3), which confirms the predictive power of the model.

Despite the obvious success of the AC model, its predictive accuracy needs to be verified by numerical solutions of the problem which would consider both the geometrical constrains as e.g. in the 2D ODIN approach developed by Pragnell et al. [11,40] and the  $\alpha\text{-to-}\gamma$  transformation as e.g. in CALPHAD-based models developed by Pillai et al. [44] or Nijdam et al. [45]. It needs to be mentioned that the AC model describes only a simplified case of chemical failure in static air not considering i) oxide spallation due to thermal cycling, ii) volatilization of  $\text{Cr}_2\text{O}_3$  in humid environments, iii) transport constraints due to

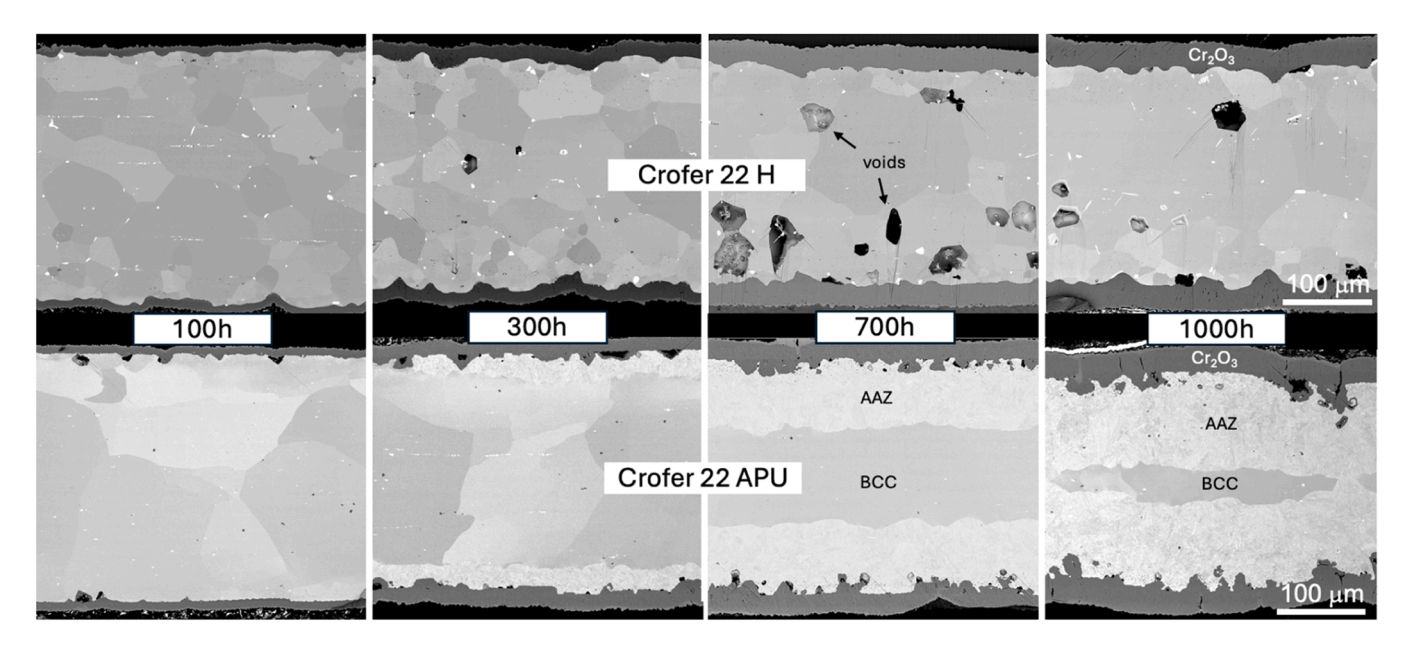
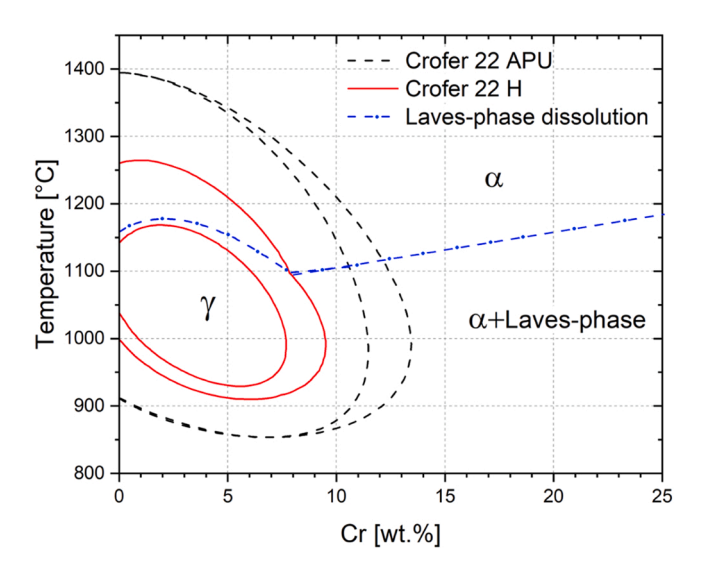


Fig. 15. Microstructural evolution in 0.3 mm thick Crofer 22 APU and Crofer 22 H foils during air oxidation for up to 1000 h at  $1000^{\circ}\text{C}$ . AAZ marks austenitization affected zone.



 $\textbf{Fig. 16.} \ \ \text{Austenite loop in Fe-Cr binary phase diagram calculated with Thermo-Calc using TCFE9 database.}$ 

complex geometries, etc. Furthermore, it is not yet clear to what extent the model is transferable to other ferritic steels suffering from austenitization, e.g. AISI 430 vs AISI 441. More experimental research is required in the future to validate the AC model and explore its applicability to realistic industrial exposure conditions.

# 5. Conclusions

Air oxidation of thin foils (0.2–0.3 mm thick) of steel grades Crofer 22 APU and Crofer 22 H has been studied for up to 2000 h at 900–1050  $^{\circ}$ C. Both steel grades suffer from premature breakaway oxidation. Accelerated oxidation of Fe initiates at the corners and edges of the foils while the Cr reservoir of the foils is far from being exhausted: the remnant Cr concentration at the oxide-metal interface in the middle of the foils varied from 17 to 21 wt%.

Crofer 22 APU is generally more susceptible to breakaway oxidation than Crofer 22 H. At 950–1050 °C, time to breakaway, t<sub>B</sub>, for Crofer 22 H was factor of 5–7 higher compared to Crofer 22 APU. At 900 °C, Crofer 22 H remained fully protective during the entire exposure for 2000 h while Crofer 22 APU suffered from premature breakaway oxidation after 700 h.

Table 3
Calculation of time to breakaway  $t_B$  using three models: mass-balance (MB) model (Eq. 1), reduced Whittle (RW) model (Eq. 3), and austenitization of corners (AC) model (Eq. 3). The kinetic input parameters  $k_c$  and D are from Table 2 and Data supplement for 950 and 1050°C. The failure criteria for MB and RW were set as  $N_{C}^{crit}$  = 0.11. For the AC calculation, the failure criterion was the concentration of austenitization determined from the phase diagram in Fig. 16. The calculated  $t_B$  values are compared with the experimental ones as well as the failure Cr-concentrations  $N_{C}^{crit}$  are compared with the experimentally measured Cr-interface concentrations  $N_{C}^{int,*}$ .

Alloy	T [°C]	$t_B$ [h]			Experimental		Input parameters			
					t <sub>B</sub> [h]	$N_{Cr}^{ m int,*}$	$N_{Cr}^0$	N <sup>crit</sup> Cr	N <sup>aust</sup> Cr	l [mm]
		MB Eq. 1	RW Eq. 2	AC Eq. 3				MB/RW	AC	
Crofer 22 APU	900	3454	3338	710	750	0,19	0,24	0,11	0,13	0,20
Crofer 22 APU	950	1340	1139	264	250	0.19	0,24	0,11	0,15	0,30
Crofer 22 H	950	4104	3903	1185	1200	0.19	0,24	0,11	0,09	0,30
Crofer 22 APU	1000	1528	1403	119	100	0,22	0,24	0,11	0,15	0,29
Crofer 22 H	1000	2278	2278	707	700	0,20	0,24	0,11	0,09	0,29
Crofer 22 APU	1050	281	256	63	50	0,20	0,24	0,11	0,15	0,30
Crofer 22 H	1050	889	863	266	300	0,20	0,24	0,11	0,08	0,30

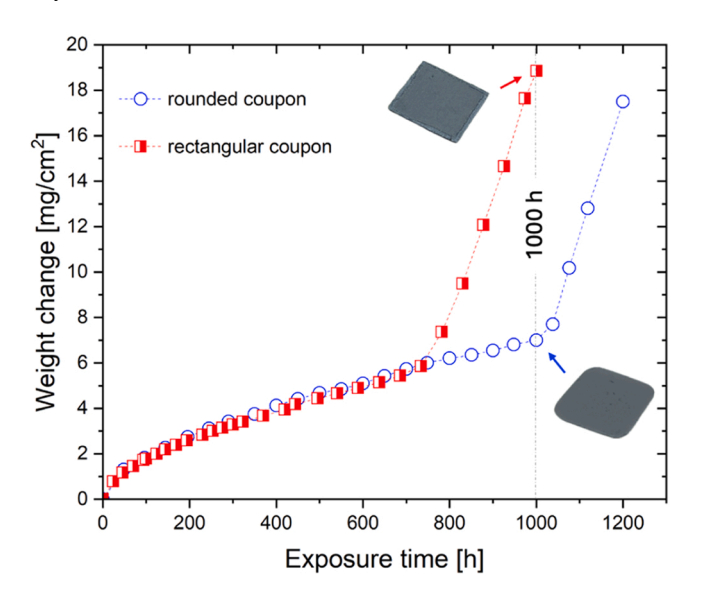


Fig. 17. Weight change for 0.3 mm thick foils of Crofer 22 H discontinuously exposed in air for up to 1200 h at  $1000^{\circ}$ C. Rectanglurar coupons (squares) are compared with rounded specimens (circles). Insets demonstrate macro images of the respective specimens after 1000 h at  $1000^{\circ}$ C.

- The initial Cr content in both alloys is virtually identical, and Crofer 22 APU oxidizes only slightly faster than Crofer 22 H, the effect being more pronounced at 900 °C. This difference is not the reason of for the initiation of breakaway oxidation
- Austenitization occurring in the Fe-Cr system above 850 °C is demonstrated to be the main trigger of breakaway oxidation.
   Alloying with ferrite stabilizing elements (Nb, W, Si in the case of Crofer 22 H) significantly extends time to breakaway.
- Classical lifetime prediction models such as Quadakkers mass-balance (MB) or Whittle depletion model (WD) systematically overpredict time to breakaway for both Crofer 22 APU and Crofer 22 H and cannot explain the difference in  $t_B$  between them. Furthermore, these models assume a critical Cr concentration of  $\sim 10$  % that is based on empirical observations but not founded in thermodynamics.
- A novel approach based on MB and WD is proposed. Two major corrections were introduced into the existing models: i) Cr depletion is considered in the corners of the foils and ii) the failure criterion is re-defined as the austenitization threshold determined from the phase diagram relevant for each individual steel grade.
- This new model describing austenitization of corners (AC) predicts very accurately the time to breakaway oxidation for both Crofer 22 APU and Crofer 22 H and quantitatively demonstrates how alloying with ferrite stabilizer, contracting the  $\gamma$ -loop, decreases the austenitization threshold and thus extends the lifetime (the case of Crofer 22 H).

# **Author contributions**

Both authors contributed to the study conception. The study design, all experiments, material preparation and data collection were performed by AC. The first draft of the manuscript was written by AC. JF commended the previous version of the manuscript. The authors read and approved the final manuscript.

# CRediT authorship contribution statement

**Anton Chyrkin:** Writing – review & editing, Writing – original draft, Visualization, Validation, Project administration, Methodology, Investigation, Funding acquisition, Formal analysis, Data curation,

Conceptualization. **Jan Froitzheim:** Writing – review & editing, Conceptualization.

#### **Declaration of Competing Interest**

The authors declare that they have no known competing financial interests or personal relationships that could have appeared to influence the work reported in this paper.

#### Acknowledgements

This work was funded by the European Union, project MSCA4Ukraine, grant No. 1232975. The present publication reflects only the author's views, and the European Union is not liable for any use that may be made of the information contained therein.

#### Appendix A. Supporting information

Supplementary data associated with this article can be found in the online version at doi:10.1016/j.corsci.2025.113260.

# Data availability

Data will be made available on request.

#### References

- W.J. Quadakkers, J. Piron-Abellan, V. Shemet, L. Singheiser, Metallic interconnectors for solid oxide fuel cells-a review, Mater. High. Temp. 20 (2003) 115–127
- [2] X. Wang, X. Shen, Research progress of ODS FeCrAl Alloys-A review of composition design, Materials 16 (2023) 6280.
- [3] G. Pauletto, A. Vaccari, G. Groppi, et al., FeCrAl as a catalyst support, Chem. Rev. 120 (2020) 7516–7550.
- [4] I. Fedorova, M. Kjellen, S. Saleem, D. Karlsson, F. Meurling, R. Berglund, Oxidation behavior of additively manufactured Ti-added FeCrAl alloys, High. Temp. Corros. Mater. 101 (2024) 1155–1165.
- [5] K.O. Gunduz, A. Visibile, M. Sattari, et al., The effect of additive manufacturing on the initial high temperature oxidation properties of RE-containing FeCrAl alloys, Corros. Sci. 188 (2021) 109553.
- [6] W.J. Quadakkers, D. Naumenko, E. Wessel, V. Kochubey, L. Singheiser, Growth rates of alumina scales on Fe-Cr-Al alloys, Oxid. Met. 61 (1) (2004) 17–37, 61.
- [7] W.J. Quadakkers, A. Elschner, W. Speier, H. Nickel, Composition and growth mechanisms of alumina scales on FeCrAl-based alloys determined by SNMS, Appl. Surf. Sci. 52 (1991) 271–287.
- [8] D.P. Whittle, Spalling of protective oxide scales, Oxid. Met. 4 (1972) 171–179.
- [9] W.J. Quadakkers, M.J. Bennett, Oxidation induced lifetime limits of thin walled, iron based, alumina forming, oxide dispersion strengthened alloy components, Mater. Sci. Technol. 10 (1994) 126–131.
- [10] W.J. Quadakkers, D. Naumenko, S. Weinbruch, I. Gurrappa, Factors governing breakaway oxidation of FeCrAl-based alloys, Mater. Corros. 51 (2000) 224–235.
- [11] W.M. Pragnell, H.E. Evans, A finite-difference model to predict 2D depletion profiles arising from high temperature oxidation of alloys, Model Simul. Mat. Sci. Eng. 14 (2006) 733–740.
- [12] W.J. Quadakkers, K. Bongartz, The prediction of breakaway oxidation for alumina forming ODS alloys using oxidation diagrams, Mater. Corros. 45 (1994) 232–241.
- [13] D.P. Whittle, The oxidation of finite samples of heat-resistant alloys, Corros. Sci. 12 (1972) 869–872.
- [14] Cowen H.C., Webster S.J. Chromium depletion during oxidation of stainless steel foils. Proceedings of the British Nuclear Energy Society international conference at Reading University, 23-24 September 1974, p. 349-358.
- [15] R. Bauer, M. Baccalaro, L.P.H. Jeurgens, M. Pohl, E.J. Mittemeijer, Oxidation behavior of Fe-25Cr-20Ni-2.8Si during isothermal oxidation at 1,286 K; Life-time prediction, Oxid. Met. 69 (2008) 265-285.
- [16] H.E. Evans, A.T. Donaldson, Silicon and chromium depletion during the Long-Term oxidation of Thin-Sectioned austenitic steel, Oxid. Met. 50 (1998) 457–475.
- [17] R. Pillai, H. Ackermann, K. Lucka, Predicting the depletion of chromium in two high temperature ni alloys, Corros. Sci. 69 (2013) 181–190.
- [18] D.J. Young, A. Chyrkin, W.J. Quadakkers, A simple expression for predicting the oxidation limited life of thin components manufactured from FCC high temperature alloys, Oxid. Met. 77 (2012).
- [19] P. Huczkowski, N. Christiansen, V. Shemet, J. Piron-Abellan, L. Singheiser, W. J. Quadakkers, Oxidation limited life times of chromia forming ferritic steels, Mater. Corros. 55 (2004) 825–830.
- [20] C. Asensio-Jimenez, L. Niewolak, H. Hattendorf, et al., Effect of specimen thickness on the oxidation rate of high chromium ferritic steels: the significance of intrinsic alloy creep strength, Oxid. Met. 79 (2013) 15–28.

- [21] P. Huczkowski, S. Ertl, J. Piron-Abellan, et al., Effect of component thickness on lifetime and oxidation rate of chromia forming ferritic steels in low and high po 2 environments, Mater. High. Temp. 22 (2005) 253–262.
- [22] D. Koszelow, M. Makowska, F. Marone, J. Karczewski, P. Jasiński, S. Molin, High temperature corrosion evaluation and lifetime prediction of porous Fe22Cr stainless steel in air in temperature range 700–900 °C, Corros. Sci. 189 (2021) 109589.
- [23] D. Koszelow, M. Makowska, F. Marone, et al., Pre-oxidation of porous ferritic Fe22Cr alloys for lifespan extension at high-temperature, Corros. Sci. 234 (2024) 112129.
- [24] A. Chyrkin, J. Froitzheim, J. Zurek, D. Naumenko, Austenitization triggering breakaway oxidation of FeCr-base alloys at 900 °C, Corros. Sci. 244 (2025) 11005
- [25] A. Chyrkin, J. Froitzheim, W.J. Quadakkers, Transition from internal to external oxidation in binary Fe–Cr alloys around 900 °C, High. Temp. Corros. Mater. 102 (2025) 1–22
- [26] O.K. von Goldbeck, Iron—Chromium Fe—Cr, IRONBin. Phase Diagr. (1982) 31–34, https://doi.org/10.1007/978-3-662-08024-5 17.
- [27] J. Froitzheim, Ferritic steel interconnectors and their interactions with Ni base anodes in solid oxide fuel cells (SOFC), Germany (2008).
- [28] B. Kuhn, C.A. Jimenez, L. Niewolak, et al., Effect of laves phase strengthening on the mechanical properties of high cr ferritic steels for solid oxide fuel cell interconnect application, Materials Science Engineering A 528 (2011) 5888–5899.
- [29] C. Asensio, A. Chyrkin, L. Niewolak, et al., Subsurface depletion and enrichment processes during oxidation of a high chromium, Laves-Phase strengthened ferritic steel, Electrochem. SolidState Lett. (2011) 14.
- [30] J. Zurek, G.H. Meier, E. Essuman, M. Hänsel, L. Singheiser, W.J. Quadakkers, Effect of specimen thickness on the growth rate of chromia scales on Ni-base alloys in high- and low-pO2 gases, J. Alloy. Compd. 467 (2009) 450–458.
- [31] P.I. Williams, R.G. Faulkner, Chemical volume diffusion coefficients for stainless steel corrosion studies, J. Mater. Sci. 22 (1987) 3537–3542.
- [32] C. Wagner, Oxidation of alloys involving noble metals, J. Electrochem Soc. 103 (1956) 571.

- [33] D.P. Whittle, G.C. Wood, D.J. Evans, D.B. Scully, Concentration profiles in the underlying alloy during the oxidation of iron-chromium alloys, Acta Metall. 15 (1967) 1747–1755.
- [34] H.E. Evans, A.T. Donaldson, T.C. Gilmour, Mechanisms of breakaway oxidation and application to a chromia-forming steel, Oxid. Met. 52 (1999) 379–402.
- [35] R.C. Lobb, J.A. Sasse, H.E. Evans, Dependence of oxidation behaviour on silicon content of 20%Cr austenitic steels, Mater. Sci. Technol. 5 (1989) 828–834.
- [36] C. Wagner, Reaktionstypen bei der oxydation von legierungen, Z. Fur Elektrochem. 63 (1959) 772–790.
- [37] J. Froitzheim, G.H. Meier, L. Niewolak, et al., Development of high strength ferritic steel for interconnect application in SOFCs, J. Power Sources 178 (2008) 163–173.
- [38] W.J. Quadakkers, P. Huczkowski, D. Naumenko, et al., Why the growth rates of alumina and chromia scales on thin specimens differ from those on thick specimens, Mater. Sci. Forum 595 (598) (2008) 1111–1118.
- [39] Thermo-Calc, TCFE6 TCS Steels/FeAlloy. Database Version 6 (2) (2013).
- [40] W.M. Pragnell, H.E. Evans, Chromium depletion at 2-dimensional features during the selective oxidation of a 20Cr-25Ni austenitic steel, Oxid. Met. 66 (2006) 209–230.
- [41] R. Sachitanand, J.E. Svensson, J. Froitzheim, The influence of cr evaporation on long term cr depletion rates in ferritic stainless steels, Oxid. Met. 84 (2015) 241–257.
- [42] D.J. Young, A. Chyrkin, J. He, D. Grüner, W.J. Quadakkers, Slow transition from protective to breakaway oxidation of haynes 214 foil at high temperature, Oxid. Met. 79 (2013).
- [43] A. Chyrkin, N. Mortazavi, M. Halvarsson, D. Grüner, W.J. Quadakkers, Effect of thermal cycling on protective properties of alumina scale grown on thin haynes 214 foil, Corros. Sci. 98 (2015).
- [44] R. Pillai, A. Chyrkin, W.J. Quadakkers, Modeling in high temperature corrosion: a review and outlook, Oxid. Met. 96 (2021).
- [45] T.J. Nijdam, L.P.H. Jeurgens, W.G. Sloof, Effect of partial oxygen pressure on the initial stages of high-temperature oxidation of γ-NiCrAl alloys, Mater. High. Temp. 20 (2003) 311.